All-Sky Image Fusion for a Synoptic Survey Telescope in Arctic and Antarctic Domains

Mariusz E. Grøtte, Shahzad Virani

Graduate Research Assistant, School of Aerospace Engineering, Georgia Institute of Technology

Marcus J. Holzinger

Assistant Professor, School of Aerospace Engineering, Georgia Institute of Technology

Andrew Register

ELSYS Chief Scientist, Principal Research Engineer, Georgia Tech Research Institute

Claudio A. Perez

Professor, Department of Electrical Engineering and Advanced Mining Technology Center, Universidad de Chile

Juan E. Tapia

Research Scientist, Research Scientist, Department of Engineering Science, Universidad Andres Bello

Abstract

Near-Earth object (NEO) detection, transient astronomical event detection, and Space Situational Awareness (SSA) support are all provided by wide-field, high cadence synoptic telescope surveys. Many such exquisite and monolithic synoptic surveys achieve impressive performance and are certainly changing these application areas. In the past 15 years Raven-class telescopes have made a clear case for the utility of commercial-off-the-shelf systems in SSA. This paper documents the initial efforts and next steps for the Omnidirectional Space Situational Awareness (OmniSSA) array, a wide-field-of-view synoptic survey system that leverages the Raven-class telescope paradigm. The approach utilizes multiple overlapping wide field-of-view sensors with post-processing super resolution and image stacking techniques to generate synthetic images equivalent to larger wide field-of-view systems. The synthetic array offers potential to utilize a plurality of components that are individually low cost and commercial-off-the-shelf. A brief survey of synoptic survey systems is presented, followed by a description of the current hardware implementation of the OmniSSA array and preliminary out-of-the-box results for baseline OmniSSA camera SR and image stacking routines.

1 Introduction

Several telescope applications including detecting near-Earth objects (NEOs), detecting transient astronomical events (supernovae, gamma ray bursts), and supporting space situational awareness (SSA) activities all necessitate observing large regions of the celestial sphere at high cadences.

There have been over 14,805 NEOs detected, of which 874 are larger than 1km in diameter.[1] Because NEOs, defined as objects with perihelion ≤ 1.3 AU and aphelion ≥ 0.983 AU, have Earth-crossing orbits, they naturally motivate substantial efforts to detect, classify, and characterize

[1] `http://neo.jpl.nasa.gov/stats/`, accessed Sep. 14, 2016

them [1]. Extrapolation of these detections accounting for the true estimated distribution of NEOs suggests that there are 981 $\pm$ 19 NEOs larger than 1km, and potentially 20,500 $\pm$ 3,000 NEOs larger than 100m [2]. To place these statistics in perspective, the recent Chelyabinsk airburst event is thought to be the result of a 20m diameter meteor entering the Earth's atmosphere at approximately 19 km/s [3]. With relatively small asteroids capable of inflicting substantive damages, there is significant motivation to detect a larger fraction of the NEO population.

So-called 'time-domain' astronomy has undergone significant growth in the past two decades. Supernovae (SNe) and gamma ray burst events are two examples of extremely transient events, and variable stars are examples of relatively transient events. Other motivations are to search for theoretically predicted events, in particular fallback supernovae, macronovae, Ia supernovae, and gamma-ray burst afterglows [4]. Further studies of these events can yield deeper cosmological and astronomical insights and understandings, including important properties such as the Hubble constant [5]. The primary problem in executing such studies is the timely detection of events when their location in the celestial sphere is unknown until they occur [4]. This motivates very wide FoV sensors and search patterns producing regular celestial sphere coverage.

The purpose of Space Domain Awareness (SDA) is to provide decision-makers with quantifiable and timely evidence of behavior(s) attributable to specific space domain threats and hazards. A foundational input to SDA activities are direct optical, radar, and other observations of on-orbit objects. There are presently in excess of 17,000 space objects larger than 10cm in Earth orbit. Of these, more than 1,100 are active spacecraft. To maintain orbit estimates on this population, the United States Space Surveillance Network (SSN) makes 380,000 to 420,000 optical and radar observations each day[2]. There is in general a tremendous need for persistent un-cued detection and tracking support for SDA activities; for optical sensors, this need again points towards wide-field of view systems capable of generating high accuracy inertial bearing and photometric brightness measurements.

Surveys with large area of coverage and short revisit times are called synoptic telescope surveys and have motivated the design and construction of substantial numbers telescope systems over the past several decades. Quickly covering large tracts of the sky suggests several telescope design architectures, of which exquisite telescope arrays and wide FoV telescopes are popular choices [6]. Example systems include the Catalina real-time transient survey (RTTS) [7], SkyMapper [8], Pan-starrs [9], Space Surveillance Telescope (SST) [10], Zwicky Transient Factory (ZTF) [11], Large Synoptic Survey Telescope (LSST) [12, 13], Dragonfly [14], and Evryscope [15]. Most of these telescope architectures intentionally avoid overlapping sensor fields of regard, preferring instead to form mosaic patterns during the course of their surveys.

Ultra-wide FoV systems, such as AllSky cameras with fields of view up to 190°, are often not considered for synoptic survey tasks because of their small collecting areas, poor angular resolution, and image distortion characteristics. However, recent advances in computer vision and image processing show great promise in enabling ad-hoc collections of these AllSky sensors to serve many synoptic survey functions. Further, the Raven-class telescope philosophy is only beginning to manifest in the world of synoptic telescope surveys.

The Air Force Research Laboratory (AFRL) Directed Energy Directorate began the Raven project in 1995 at the Air Force Maui Optical and Supercomputing (AMOS) site [16]. A Raven-

[2] `http://www.stratcom.mil/factsheets/11/Space_Control_and_Space_Surveillance/`, accessed April 29, 2015

class system is composed of commerically available equipment (e.g., telescope, electro-optical sensor, dome, weather station, GPS receiver) to form a high-functioning system capable of many routine Space Surveillance Network (SSN) tasks. Telescopes conforming to this high level approach are often called Raven-class Telescopes [16, 17].

The effort discussed in this paper is a re-examination of AllSky optical sensors, particularly with respect to NEO detection, time-domain astronomy, and SSA. Fundamental questions include: 1) Can the Raven-class telescope paradigm be extended to synoptic survey telescopes, enabling a subset of synoptic survey telescope activities to be conducted by lower cost COTS systems? 2) Can recent advances in computer vision and astronomy image processing enable a new class of non-exquisite, Raven-like synoptic survey telescopes?

Image stacking techniques (e.g., averaging, median, $\sigma-$clipping) have long been used to improve overall system signal-to-noise ratio [18] for sequential measurements using the same sensor. Intuitively, image stacking techniques may also be employed for *simultaneous* observations made by very similar sensors with overlapping fields of regard. The Dragonfly telescope certainly innovates in this direction for looking at very dim objects using a plurality of commercial-off-the-shelf (COTS) Cannon lenses and SBIG cameras [14]. Parallel to the technological development of improved sensors and commercialization of high quality small diameter telescopes (< 0.6m), critical new innovations have been made by computer scientists in super-resolution (SR) techniques. Using multiple low resolution input images, SR techniques infer higher resolution images [19, 20, 21, 22]. SR methods are well-known in astronomy and have been used to directly identify binary stars using sequential measurements [23].

Neither of SR nor image stacking methods have been fused together in to a single unified algorithm tailored to ingest large numbers of *simultaneous* overlapping ultra-wide FoV images ($\pi/2$ to 2π steradians) to improve both the detected object SNR, angular resolution, and bit-depth of the aggregated synthetic sensor.

The architecture proposed in this paper consists of a plurality of ultra wide FoV (FoV) electro-optical sensors with overlapping fields of regard (covering a sizable fraction of the night sky, between $\pi/3$ and 2π steradians). Frames can be exposed simultaneously and post processing algorithms (frame stacking, super-resolution) employed to create synthetic images for synoptic survey purposes. Such an approach is in direct contrast to mosaic survey approaches and allows an array of COTS systems to perform routine (though, clearly not all) synoptic survey tasks at high cadences for potentially reduced cost. If a modular design and assembly-line style manufacturing approach is taken, then with sufficient computing resources the capability of such a synthetic array may scale favorably.

This paper contains the following elements: 1) a brief survey of synoptic survey systems, 2) A description of the current hardware implementation of Georgia Tech's Omnidirectional SSA (OmniSSA) array, and 3) preliminary out-of-the-box results for OmniSSA camera SR and image stacking.

2 Review of selected synoptic survey telescopes

A brief review of selected synoptic survey telescopes is included to provide context for the niche that OmniSSA serves. Table 1 identifies such systems in chronological order of first-light, and contains the FoV, diameter, entendue, and imaging data scale for each system. Entendue, defined as the product of the solid-angle in the FoV and the area of the collecting surface, is known to be conserved throughout a telescope system and is used as a 0^{th}-order measure of the

rate of productive science for synoptic survey systems [24]. In the context of SSA entendue may be considered a gross approximation of the un-cued detection capability of a system. However entendue it is certainly not a substitute for venerable metrics such as limiting magnitude and pixel resolution, but simply indicates how rapidly the sky may be surveyed at a fixed limiting magnitude. Note, for OmniSSA in particular, the limiting magnitude in question may be quite bright, however because it has such a wide FoV it is capable of surveying the night sky relatively quickly.

Table 1: Comparison of Selected Synoptic Survey Systems

System	**FoV** ($\deg^2$)	**Diameter** (m)	**Entendue** (m^2 $\deg^2$)	**Pixels** (Megapixels)	**Oper.** (year)
Catalina RTTS [7]	1°x 1°	1.5m	2.3	16	1970-
Siding Spring S.	3°x 3°	0.5m	2.3	16	2004-13
SkyMapper [8]	1.7°x 3.3°	1.35m	10	268	2008-
Pan-starrs [9]	3°x 3°	1.8m	29	1,400	2010-
SST [10]	3°x 2°	3.5m	74	96	2011-
ZTF [11]	6.9°x 6.9 °	1.2m	68	576	2017*
LSST [12, 13]	3.5°x 3.5°	8.4m	860	3,200	2019*
Dragonfly [14]	2°x 3°	0.46m	1.1	8.3 (x10)	2014-
Evryscope (indiv.) [15]	23.8°x 16.0°	0.061m	1.5	28	2015-
Evryscope (mosaic) [15]	90°x 90°	0.061m	32	780	2015-
OmniSSA (narrow)	66°x 82°	0.064m (0.0375*m)	13	14 (8.3*)	2016*
OmniSSA (wide)	100°x 130°	0.064m (0.0375*m)	31	14 (8.3*)	2016*

A '*' indicates a projected 'first-light.'

As the interst and funding support for synoptic surveys have risen, Table 1 captures an overall increase in Entendue and total pixels. Importantly, below the horizontal divider are three new systems (first light between 2014 and 2016) that the authors would classify as 'Raven-like' synoptic survey systems: the Dragonfly Telescope [14], the Evryscope [15], and OmniSSA.

The Dragonfly telescope consists of 10 Canon 400 mm f/2.8 L IS II USM telephoto lenses with SBIG 8300M cameras [14]. These individual low-cost COTS cameras all have overlapping FoV and image simultaneously, collectively giving an effective collecting area diameter of 0.46m. Because these are statistically independent measurements, the 10 simultaneous image measurements allow statistical interrogation of the images to detect dimmer objects than a typical 0.46m telescope.

The Evryscope also leverages a Raven-like approach by arranging 27 Rokinon 85mm f/1.4 lenses into a hemispherical mosaic pattern. Each lens is affixed to a 5-position filter wheel and a 28.8 MP KAI29050 interline-transfer CCD. Combined, the mosaic captures 8,000 $\deg^2$ images every two minutes with a limiting magnitude of 16.5 m_v. This COTS system design allows astonishingly high cadence synoptic surveys, and sports an entendue similar to Pan-starrs [15].

The OmniSSA array is combination of the Dragonfly and Evryscope approaches, and uses COTS lenses with ultra wide overlapping FoVs and post-processing to synthetically increase the effective aperture, resolution, read noise, and bit depth. While this design and preliminary results are discussed in later sections, the authors claim that Dragonfly, Evryscope, and OmniSSA are the first instances of 'Raven-like' or 'Raven-class' synoptic survey telescopes.

3 Hardware

3.1 Electro-optical sensors

All three (3) Electro-optical (EO) sensor modules each contain a Rokinon 10mm F/2.8 ED AS IF NCS lens, a SBIG FW5-8300 5-position filter wheel (presently with Johnson filters), an SBIG STF-8300M CCD, and an ODROID single-board computer (SBC). A block diagram of this configuration is depicted in Figure 1(a), while a photo of all three EO sensor modules is shown in Figure 1(b).

(a) EO sensor module block diagram

(b) EO sensor modules

(c) Partially assembled OmniSSA

Figure 1: Sensor module and partially assembled OmniSSA array

The STF-8300M has a cooled CCD with 3326 x 2504 pixels, each with a pixel pitch of 5.4μm, bit-depth of 16 bits, and read noise of 0.02 e^-/pixel/sec at -15°C. The EO sensor module design preserves the capability of simultaneous triggering through the synchronization port. [3]. The approximate pixel FoV is 106 arcsec (at the boresight) and the Rokinon lens has an effective collecting diameter of 3.75mm. It provides an ultra-wide FoV for each EO sensor module of 66°$\times$ 82°(102°corner-to-corner; verified in calibration). The ODROID units each have real-time clock shields, allowing the EO sensor modules to synchronize with one another and use either network time or GPS time to trigger exposures.

With the current prototype lens and EO sensor module design, predicted performance at Svalbard, Norway and Antarctica are shown in Figures 2(a) and 2(b), respectively. These predictions assume a 30 second integration time, 3 simultaneous observations ($\sqrt{3}$ SNR improvement), and that algorithms make detections of objects at SNR ≥ 4.

3.2 Data handling, processing, and storage

With three 8.3MP 16 bit images regularly generated every 30 seconds, potentially for months at a time, substantial data handling, processing, and storage challenges exist. An on-board Dell Mini-PC is selected to process raw images, conduct super-resolution and image stacking activities,

[3] SBIG-8300M Spec Sheet, last accessed 9/13/16
https://www.sbig.com/products/cameras/stf-series/stf/stf-8300m/

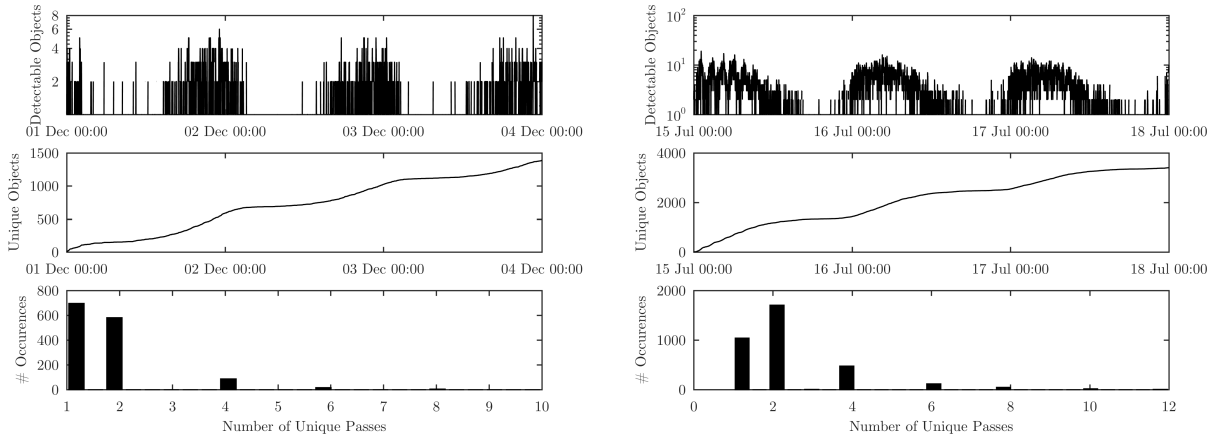

(a) Svalbard, Dec. 1, 2016

(b) Antarctica, Jul. 1, 2017

Figure 2: Predicted OmniSSA 3-day performance during arctic / antarctic winter

detect & track space objects, and compress images & tracking data. To accommodate data transfer demands, OmniSSA has adopted a distributed network architecture over Gigabit Ethernet (GE). With this system, if a single EO sensor module, harddisk, or other non-critical component fails, the system may still operate at reduced efficiency. Because of the distributed network architecture, the entire system may also be remotely controlled from the Georgia Tech operations center. Network speed and security are critical features, and OmniSSA contains its own internal 16-port GE network switch and industrial-grade GE firewall. When operating at 100% capacity at Svalbard or the antarctic OmniSSA is expected to generate 6.5 TB of compressed images, processing products, and track telemetry each month. To enable operation over extended periods without high-bandwidth internet capacity, OmniSSA contains an internal network accessible storage (NAS) drive with 32TB of RAID 0 storage (enough for 4-5 months of continuous operation).

3.3 Power supply, distribution, and system thermal control

OmniSSA is engineered to operate with both 120VAC and 220VAC (60Hz) power supplies using an external weather-hardened connector. Internally, this power is routed through a distribution strip (with limited surge protection) from which the primary computer, firewall, network switch, NAS drive, and DC power supplies draw power (each of which can transform 120VAC and 220VAC internally as needed. To power the EO sensor modules and thermal control system both 5VDC and 12VDC (TRC Electronics HRP-75-5 and HRP-300-12, respectively) power supplies are included in the design. A high-level notional block diagram of 120VAC, 5VDC, and 12VDC is included in Figure 3(c).

Thermal control is effected using a SBC with several temperature sensors, DC fans, and ohmic heating strips. In the current design the SBC is a Raspberry Pi 3 (RPi3), and interfaces with the ohmic heating strips and two McMaster-Carr 4.7" square 12V DC fans through a 4-channel relay via the RPi3 GPIO pins. The temperature sensors are Adafruit MCP9808 models (± 0.25°C over -40°C to 120°C) and interface with the RPi3 through the GPIO pins. A simple bang-bang control law keeps the system temperature (as measured through the 6 temperature sensors) within 5°C and 40°C.

(a) Isometric OmniSSA rendering

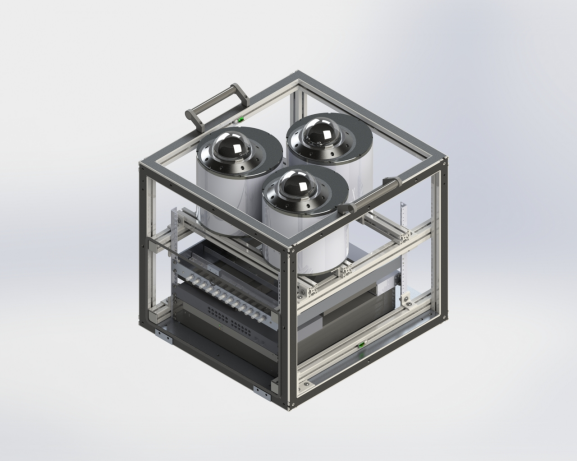

(b) Isometric OmniSSA rendering w/o skin

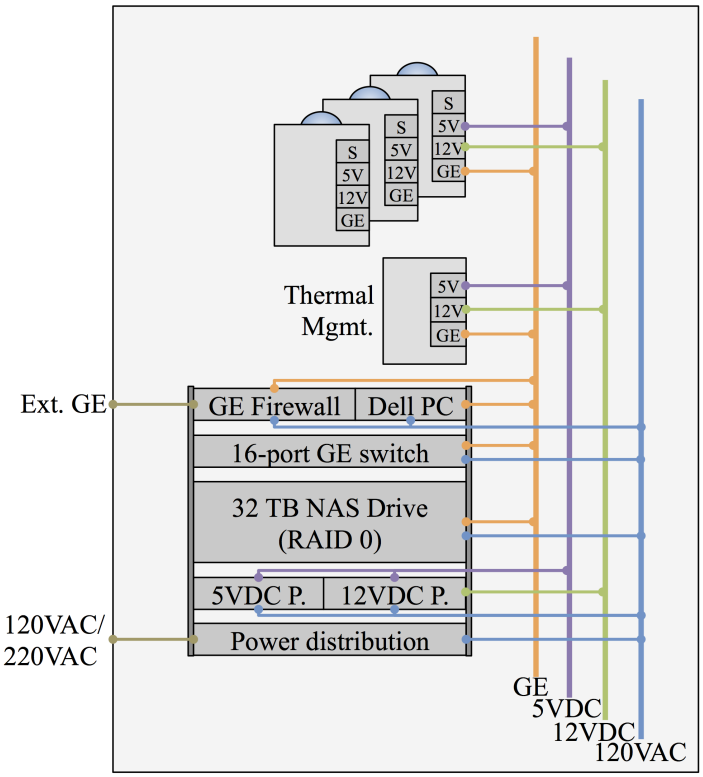

(c) OmniSSA Block diagram

Figure 3: Internal / external OmniSSA renderings and block diagrams

4 Results

This section contains initial results from the first night of observation on 30^{th} August, 2016 at 01:47:57 UTC with the OmniSSA EO sensors in downtown Atlanta (33.777468° N, 84.398969° W). All three sensors were triggered simultaneously for several consecutive frames, each with 30 second integration times. Here, only a single set of three simultaneously captured images are investigated using super resolution and frame stacking methods. Calibration and image registration

are first discussed, followed by image super resolution and frame stacking results.

4.1 Calibration and inertial image registration

Due to the nature of wide field of view lenses, light passing through the lens onto the sensor is distorted, displacing the centroids of detections in the resulting image, ultimately producing erroneous vectors. The Brown distortion model [25], given in Equation 1, relates distorted coordinates $(\cdot)_d$ to undistorted coordinates $(\cdot)_u$, using five distortion parameters, K_1, K_2, K_3, P_1, and P_2, where K_1, K_2, and K_3 quantify the radial distortion and P_1 , P_2 quantify the tangential distortion.

$$\begin{bmatrix} x_d \\ y_d \end{bmatrix} = \begin{bmatrix} x_u \\ y_u \end{bmatrix} + \begin{bmatrix} x_u r^2 & x_u r^4 & x_u r^6 & 2x_u y_u & r^2 + 2x_u^2 \\ y_u r^2 & y_u r^4 & y_u r^6 & r^2 + 2y_u^2 & 2x_u y_u \end{bmatrix} \begin{bmatrix} K_1 \\ K_2 \\ K_3 \\ P_1 \\ P_2 \end{bmatrix} \tag{1}$$

$$r^2 = x_u^2 + y_u^2 \tag{2}$$

Since Equation (1) is not invertible in x_u and y_u, the Newton-Raphson method is used to infer the undistorted coordinates. Letting $\mathbf{f}(x_u, y_u)$ be the right hand side of Equation (1), define a new function $\mathbf{g}(x_u, y_u) = \mathbf{f}(x_u, y_u)[x_d, y_d]^T$. The sequence given in Equation (4) quickly converges, yielding the best-fit undistorted coordinates, where $\mathbf{J}$ is the Jacobian matrix of $\mathbf{g}$.

$$\begin{bmatrix} x_u \\ y_u \end{bmatrix}_n = \begin{bmatrix} x_u \\ y_u \end{bmatrix}_{n-1} - \mathbf{J}^{-1}\mathbf{g} \tag{3}$$

To calibrate the lenses and the cameras, a checkerboard pattern was projected onto a large screen and various images were taken with the camera in different orientations to map the distortion field in the entire image as shown in Figure 4(a) and 4(b). Since the size of the squares were known, the intrinsic and extrinsic properties along with the distortion coefficients of the lens were determined using the Image Processing Toolbox in MATLAB. Table 2 shows the results for the focal length and distortion coefficients form all three camera systems.

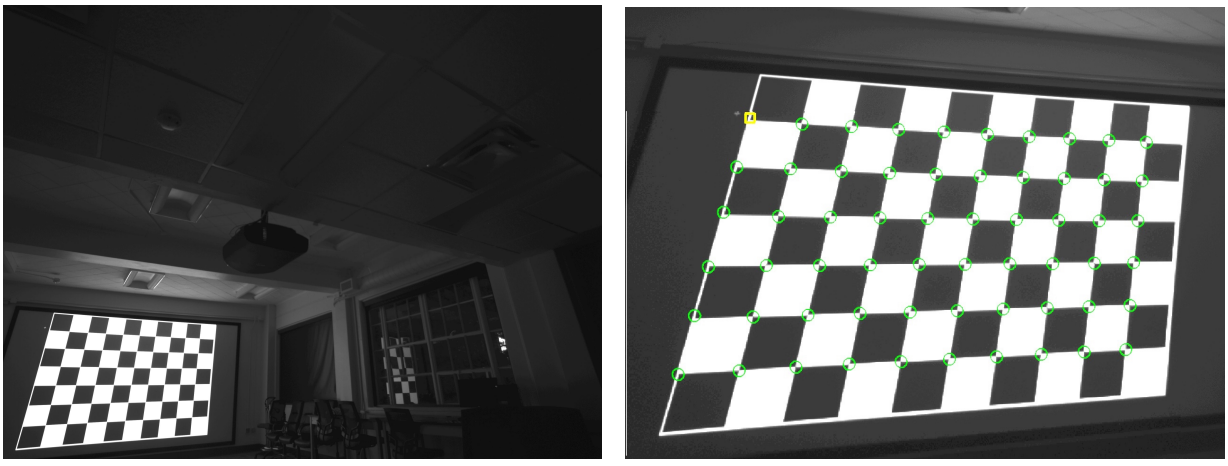

(a) Calibration image taken by OmniSSA Camera 1. (b) Part of the calibration image with corners detected.

Figure 4: Calibration images for OmniSSA.

Table 2: Calibration Results with 95% Confidence Interval

Parameters	Camera 1		Camera 2		Camera 3	
	Value	Confidence	Value	Confidence	Value	Confidence
f(px)	1949.98	7.252	1955.70	5.323	1935.95	8.443
K_1	$-2.573e^{-2}$	$2.445e^{-3}$	$-1.9627e^{-2}$	$1.814e^{-3}$	$-1.862e^{-2}$	$2.912e^{-3}$
K_2	$-1.234e^{-2}$	$3.978e^{-3}$	$-2.0326e^{-2}$	$2.842e^{-3}$	$-2.408e^{-2}$	$4.498e^{-3}$
K_3	$1.266e^{-2}$	$2.924e^{-3}$	$1.6425e^{-2}$	$1.948e^{-3}$	$1.968e^{-2}$	$2.988e^{-3}$
P_1	$-4.972e^{-3}$	$4.242e^{-4}$	$-4.2465e^{-3}$	$3.297e^{-4}$	$-4.216e^{-3}$	$5.339e^{-4}$
P_2	$-1.862e^{-3}$	$6.119e^{-4}$	$-1.7941e^{-3}$	$4.558e^{-4}$	$-4.114e^{-5}$	$7.503e^{-4}$

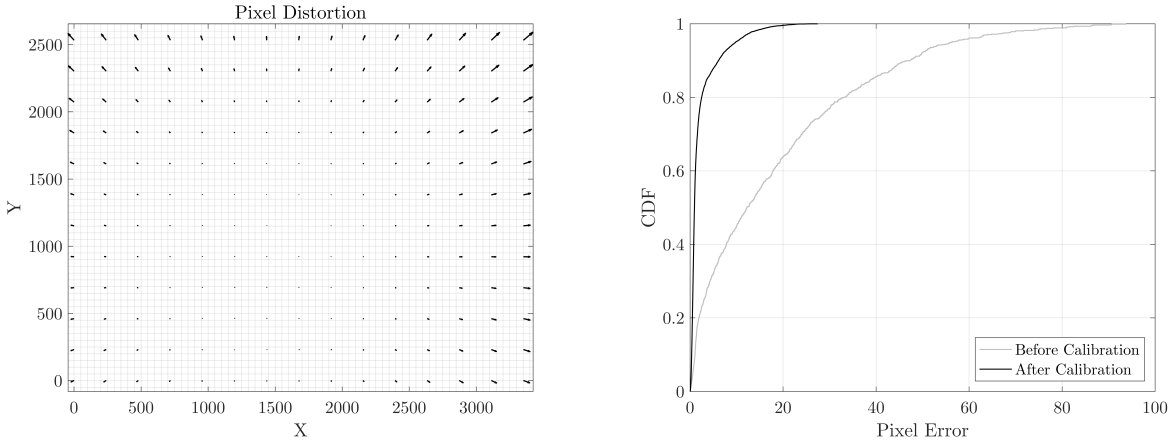

(a) Distortion Field of Camera 1 on OmniSSA.

(b) Cumulative Distribution Function of the post calibration pixel error.

Figure 5: Distortion field and residual pixel error for OmniSSA Camera 1.

Tools from Astrometry.net [26] are used on the undistorted frames to positively identify stars within the field of view using blind astrometric calibration routines. While blind astrometric calibration routines such as those found in Astrometry.net do not need undistorted images in general, the distortion in the Rokinon lenses used by OmniSSA is sufficient to cause problems in this process if unaided. After this process the individual images are registered against the inertial frame. Such an image along with star catalog number overlay is given in Figure 6. The distortion field and pre-/post- calibration residual errors are shown in Figures 5(a) and 5(b), respectively.

There are several streaks within the image in Figure 6 that can be seen by the unaided eye. Comparing with the two-line elements (TLEs) from the public Space Object Catalog[4], there are several likely correlations, namely COSMOS 2084 and H-2A R/B (crossing near RA=120°and DEC=5°). There are two other streaks in the image (near RA=55°and DEC=45°) both are airplanes at different altitudes based on their streak length and thickness. Note that the image in Figure 6 is inverted for clarity.

[4]Last accessed September, 2016: `https://www.space-track.org/`

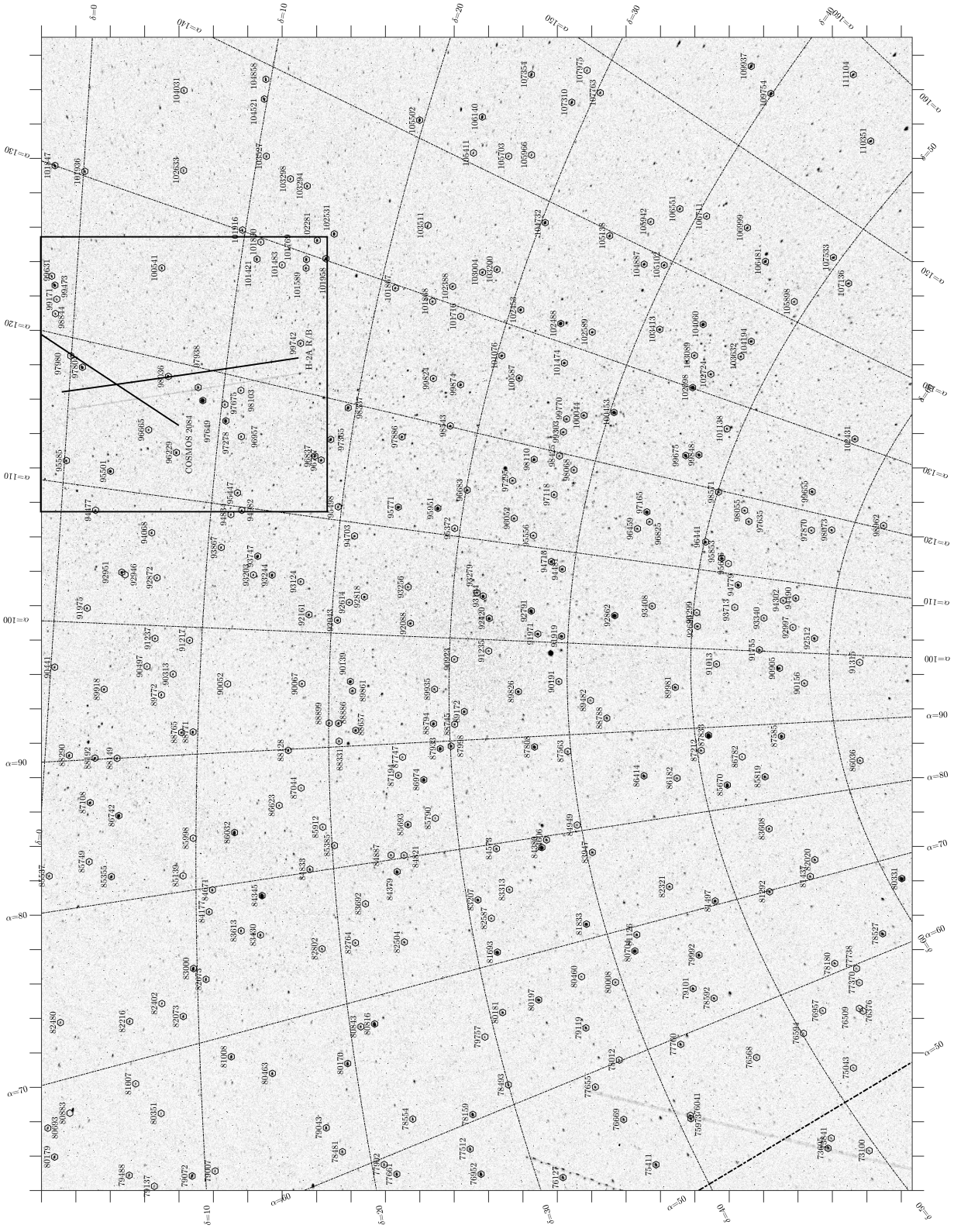

Figure 6: Inverted Image from Camera 1 on OmniSSA. The square box shows the area of interest for Super Resolution and Image Stacking Algorithms. The black lines along with the space object name represent the expected locations for the tracks determined from the TLEs.

4.2 SNR improvement using image stacking techniques

One of the ways to improve the signal-to-noise ratio of a signal in an image is by using image stacking techniques. This method involves taking multiple exposures of the same field of view and use additive stacking techniques for noise reduction. Typically, this is done by taking short exposures of a target using a single camera. Since OmniSSA's main goal is to detect and track space objects, the platform uses three cameras to simultaneously image the moving objects. The position and orientation of three cameras and lenses differ. Hence, image registration techniques are required to first align the images together before stacking the images. After the images are aligned and the background is subtracted, a frequency domain approach by Vandewalle [27] is used to register the images. Once, the images are aligned, simple additive stacking is used to generate the stacked image.

Table 3 shows the scaling between mosaic and synthetic apertures. Theoretically, the SNR of the signal after image stacking is expected to increase by the square root of the number of images, ~1.73, on average. Figure 7(a) shows a part of the stacked image generated from images using three OmniSSA cameras. To compare the results to the theory, SNR is computed along a row of pixels that intersects the streaks and is denoted by a black line in the figure. SNR is computed using Equation 4, where $\mathbf{E}(S_i)$ is the expected value of the signal and σ is the standard deviation of the noise.

$$\text{SNR}_i = \frac{\mathbf{E}(S_i)}{\sigma} \tag{4}$$

Table 3: Comparison of Selected Synoptic Survey Systems

	Mosaic	Synthetic
Required Signal-to-Noise Ratio (m)	$\text{SNR}_{i,req}$	$\text{SNR}_{i,req}/\sqrt{n}$
Effective iFoV (rad)	iFoV_i/n	$\text{iFoV}_i/\sqrt{n}$
Effective shot noise (counts)	$\sigma_{r,i}$	$\sigma_{r,i}/\sqrt{n}$
Effective brightness resolution (bits)	d_i	$d_i + log_2(2n)$

Figure 7(b) shows the comparison of the SNR before and after image stacking. Theoretically, two peaks are expected in the figure where the streaks cross the selected row of pixels. It can be seen that the noise in the image is attenuated and the signal from the streaks (two peaks in the figure) is amplified. The ratio of the SNR before and after stacking the images was ~1.324. Several sources, such as errors in calibration, background subtraction and image registration, can cause this ratio to differ from theoretical value. Advanced background subtraction techniques and image registration in the angle space will significantly improve the SNR increase after stacking.

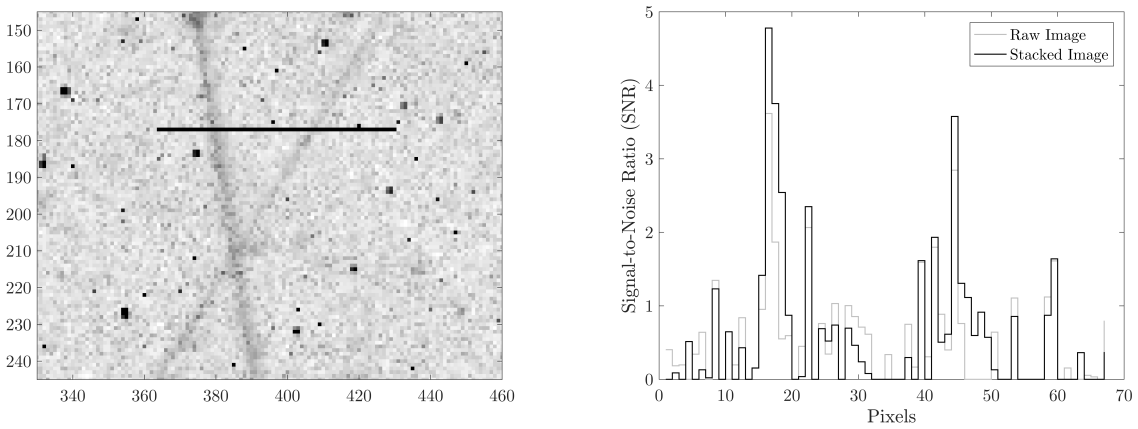

(a) The black line shows the row and columns of pixels across which the SNR was measured.

(b) Signal-to-Noise Ratio comparison before and after performing image stacking.

Figure 7: SNR Comparison before and after performing Image stacking technique.

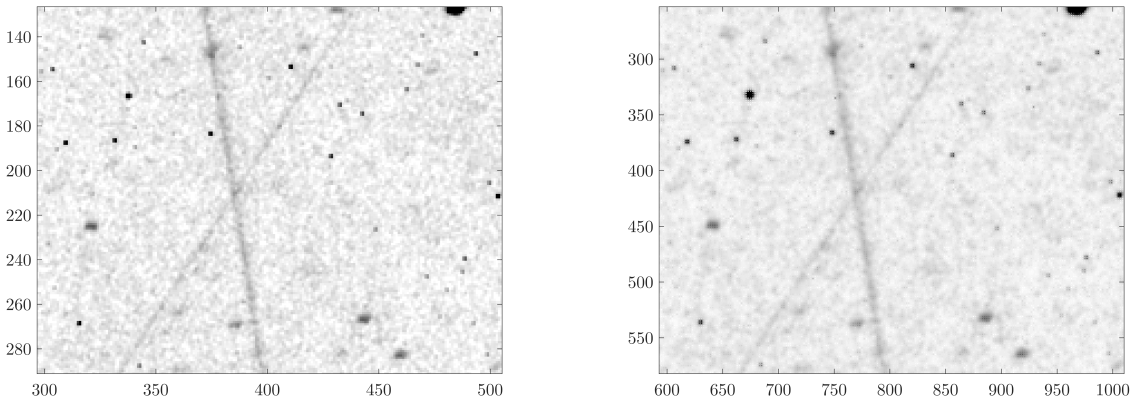

(a) Raw image before Super Resolution.

(b) Super Resolved Image using Projection onto Convex Sets technique.

Figure 8: Comparison of Raw and Super Resolved Image.

4.3 Resolution improvement using Super Resolution methods

To increase the resolution of the image, Projection on Convex Sets (POCS) based Super-Resolution image reconstruction technique is used [28]. The image is scaled by 2. Figure 8(a) shows an area of interest from one of the raw images that is used in reconstruction. The images are inverted for clarity. Figure 8(b) shows the POCS based reconstructed image using three raw images. Note that the raw and reconstructed image show the same region of interest. However, for the same region, the reconstructed image is twice as large in pixels as the raw image. Therefore, the instantaneous field of view (iFoV), which represents the field of view a single pixel can see, is decreased from 106 arcsec/pixel to 60 arcsec/pixel.

5 Conclusions

Synoptic survey systems are discussed and compared with 'Raven-like' synoptic survey telescopes. These 'Raven-like' synoptic survey telescopes, especially Evryscope and to a lesser extent OmniSSA, demonstrate substantive value to SDA using COTS hardware. Mosaic and super resolution methods strongly impact the design of synoptic survey telescopes, and should be analytically formalized into a multi-objective optimization design problem with respect to signal SNR, pixel resolution, and bit-depth. Serving as an experiment platform for synthetic synoptic AllSky surveys, OmniSSA shows promise, particularly at its economical price point. Planned observation campaigns in Svalbard, Norway and the northern peninsula on Antarctica will confirm or deny efficacy in supplementary synoptic survey efforts for transient astronomy, NEO searches, and SSA.

Acknowledgements

This work has been partially funded by AFOSR grant # FA9550-16-1-0027. The OmniSSA hardware system hardware and integration has been funded by the Georgia Tech Research Institute (GTRI). The authors would like to thank Patrick O'Connell, Lourenco de Almeida, Eric Avari, Andre Barnes, Arpit Patel, Hayden McKinley, Joshua Shuttle, Adam Holloway, Stephen Rehnberg, and Hassan Rashid at Georgia Tech for their hard work on OmniSSA as part of their M.S. and B.S. degrees in Aerospace and Mechanical Engineering.

References

[1] William F. Bottke Jr., Alessandro Morbidelli, Robert Jedicke, Jean-Marc Petit, Harold F. Levison, Patrick Michel, and Travis S. Metcalfe. Debiased orbital and absolute magnitude distribution of the near-earth objects. *Icarus*, 156(2):399 – 433, 2002.

[2] A. Mainzer et. al. Neowise observations of near-earth objects: Preliminary results. *The Astrophysical Journal*, 743(2):156, 2011.

[3] Popova et. al. Chelyabinsk airburst, damage assessment, meteorite recovery, and characterization. *Science*, 342(6162):1069–1073, 2013.

[4] Rau et. al. Exploring the optical transient sky with the palomar transient factory. *Publications of the Astronomical Society of the Pacific*, 121(886):pp. 1334–1351, 2009.

[5] Bohdan Paczyński. Monitoring all sky for variability. *Publications of the Astronomical Society of the Pacific*, 112(776):pp. 1281–1283, 2000.

[6] John L. Tonry. An early warning system for asteroid impact. *Publications of the Astronomical Society of the Pacific*, 123(899):pp. 58–73, 2011.

[7] AA Mahabal, SG Djorgovski, AJ Drake, C Donalek, MJ Graham, RD Williams, Y Chen, B Moghaddam, M Turmon, E Beshore, et al. Discovery, classification, and scientific exploration of transient events from the catalina real-time transient survey. *arXiv preprint arXiv:1111.0313*, 2011.

[8] Stefan C Keller, Brian P Schmidt, Michael S Bessell, Peter G Conroy, Paul Francis, Andrew Granlund, E Kowald, AP Oates, T Martin-Jones, T Preston, et al. The SkyMapper telescope and the southern sky survey. *Publications of the Astronomical Society of Australia*, 24(1):1–12, 2007.

[9] Nicholas Kaiser, Herve Aussel, Barry E. Burke, Hans Boesgaard, Ken Chambers, Mark R. Chun, James N. Heasley, Klaus-Werner Hodapp, Bobby Hunt, Robert Jedicke, D. Jewitt, Rolf Kudritzki, Gerard A. Luppino, Michael Maberry, Eugene Magnier, David G. Monet, Peter M. Onaka, Andrew J. Pickles, Pui Hin H. Rhoads, Theodore Simon, Alexander Szalay, Istvan Szapudi, David J. Tholen, John L. Tonry, Mark Waterson, and John Wick. Pan-starrs: A large synoptic survey telescope array, 2002.

[10] D Monet, T Axelrod, C Claver, T Blake, R Lupton, E Pearce, R Shah, and D Woods. Rapid cadence collections with the space surveillance telescope. Technical report, DTIC Document, 2012.

[11] Law et. al. The palomar transient factory: System overview, performance, and first results. *Publications of the Astronomical Society of the Pacific*, 121(886):pp. 1395–1408, 2009.

[12] J. Anthony Tyson. Large synoptic survey telescope: Overview, 2002.

[13] V. L. Krabbendam and D. Sweeney. The large synoptic survey telescope preliminary design overview, 2010.

[14] Roberto G. Abraham and Pieter G. van Dokkum. Ultra-low surface brightness imaging with the dragonfly telephoto array. *Publications of the Astronomical Society of the Pacific*, 126(935):55, 2014.

[15] Nicholas M Law, Octavi Fors, Jeffrey Ratzloff, Philip Wulfken, Dustin Kavanaugh, David J Sitar, Zachary Pruett, Mariah Birchart, Brad Barlow, Kipp Cannon, et al. Evryscope science: exploring the potential of all-sky gigapixel-scale telescopes. *arXiv preprint arXiv:1501.03162*, 2015.

[16] Chris Sabol, K Kim Luu, Paul Kervin, Daron Nishimoto, Kris Hamada, and Paul Sydney. Recent developments of the raven small telescope program. *Advances in the Astronautical Sciences*, 112:397–416, 2002.

[17] R. D. Coder. *Multi-Objective Design of Small Telescopes and Their Application to Space Object Characterization*. PhD thesis, Georgia Institute of Technology, Atlanta, GA, August 2015.

[18] CY Zhang. Robust estimation and image combining. In *Astronomical Data Analysis Software and Systems IV*, volume 77, page 514, 1995.

[19] Sung Cheol Park, Min Kyu Park, and Moon Gi Kang. Super-resolution image reconstruction: a technical overview. *Signal Processing Magazine, IEEE*, 20(3):21–36, May 2003.

[20] J. D. van Ouwerkerk. Image super-resolution survey. *Image and Vision Computing*, 24(10):1039 – 1052, 2006.

[21] Lyndsey C. Pickup, David P. Capel, Stephen J. Roberts, and Andrew Zisserman. Bayesian methods for image super-resolution. *The Computer Journal*, 52(1):101–113, 2009.

[22] Emmanuel J. Candès and Carlos Fernandez-Granda. Towards a mathematical theory of super-resolution. *Communications on Pure and Applied Mathematics*, 67(6):906–956, 2014.

[23] B. Anconelli, M. Bertero, P. Boccacci, and M. Carbillet. Restoration of interferometric images. *Astronomy & Astrophysics*, 431(2):747–755, 2005.

[24] R. Jedicke, J. Tonry, P. Veres, D. Farnocchia, F. Spoto, A. Rest, R. J. Wainscoat, and E. Lee. ATLAS: asteroid terrestrial-impact last alert system. In *American Astronomical Society, Division for Planetary Sciences Meeting Abstracts*, volume 44, 2012.

[25] John G Fryer and Duane C Brown. Lens distortion for close-range photogrammetry. *Photogrammetric engineering and remote sensing*, 52(1):51–58, 1986.

[26] Dustin Lang, David W. Hogg, Keir Mierle, Michael Blanton, and Sam Roweis. Astrometry.net: Blind astrometric calibration of arbitrary astronomical images. *The Astronomical Journal*, 139(5):1782, 2010.

[27] Patrick Vandewalle, Sabine Süsstrunk, and Martin Vetterli. A frequency domain approach to registration of aliased images with application to super-resolution. *EURASIP Journal on applied signal processing*, 2006:233–233, 2006.

[28] Sudam Sekhar Panda, MSR Prasad, and G Jena. Pocs based super-resolution image reconstruction using an adaptive regularization parameter. *arXiv preprint arXiv:1112.1484*, 2011.